RAIN EVENT DETECTION USING THE RECEIVED BEACON SIGNAL AT KA AND Q BAND

Alef Comisso
Politecnico di Milano, Milano – DEIB Piazza Leonardo da Vinci 32, 20133 Milan, Italy,
phone: +390223993426, alef.comisso@polimi.it
Miles Turner
Politecnico di Milano, Milano – DEIB Piazza Leonardo da Vinci 32, 20133 Milan, Italy,
phone: +390223993426, milesaustin.turner@polimi.it
Lorenzo Luini
Politecnico di Milano – DEIB, Piazza Leonardo da Vinci 32, 20133 Milan, Italy,
phone: +390223993693, e-mail: lorenzo.luini@polimi.it
Carlo Riva
Politecnico di Milano – DEIB, Piazza Leonardo da Vinci 32, 20133 Milan, Italy,
phone: +390223993659, e-mail: carlo.riva@polimi.it

Abstract

Satellite communication systems are increasingly operating at higher frequencies (Ku-band and above) to meet rising data rate demands. However, higher frequencies suffer greater degradation from tropospheric impairments, particularly rain (above 10 GHz), clouds (above 30 GHz), and atmospheric gases, making static margins insufficient. Accurate characterization of tropospheric attenuation is therefore essential in SatCom designs. Propagation campaigns provide valuable data by yielding attenuation time series, which are used to characterize the SatCom channel. To produce these attenuation time series, an operator uses of various techniques to detect rainfall along the path so that specific calibration methods can be used to distinguish the attenuation effects specifically induced by rain from any system effects. This article proposes a new event detection algorithm called Rain Event Detector, that operates solely on the received beacon signal power to detect rain events along the signal trajectory. The algorithm is tested using data from the Alphasat Aldo Paraboni propagation experiment at the Italian ground stations Tito Scalo and Spino d'Adda. Validation is performed against the same dataset but calibrated with the aid of a radiometer and visual inspection. Results demonstrate that the proposed algorithm provides reliable rainfall event detection without auxiliary equipment, offering a robust alternative when radiometer data are unavailable, and enabling continued exploitation of high-frequency SatCom links under adverse tropospheric conditions.

1. Introduction

Satellite communication systems are rapidly migrating to higher frequency bands, particularly Ka-, Q-, and V-band, to satisfy the growing demand for capacity driven by broadband services, mobility, and next-generation applications [1]. While these frequencies enable larger bandwidths, they are also more susceptible to tropospheric impairments [2]. Rain produces strong attenuation above 10 GHz, clouds become significant above 30 GHz, and gaseous absorption due to water vapor and oxygen is always present [3]. The presence of clouds and rain can lead to deep fades that degrade link quality, thus effecting the overall availability and throughput. To ensure that service agreements are met accurate characterization of the propagation channel is essential when designing the system and planning fade mitigation strategies [4].

Propagation campaigns are designed to study these effects by collecting beacon power measurements from dedicated satellite payloads. Such measurements capture the combined influence of the troposphere on the Earth–space link, providing attenuation time series for analysis on various environmental conditions that could affect the link. A crucial step in these campaigns is processing the data to distinguish moments of clear-sky conditions from moments of attenuation events caused by rain and clouds. This distinction is important as it will affect how the received power signal is calibrated, i.e. how it is converted into attenuation along the link. There are many ways to calibrate the received beacon power in order to derive attenuation, such as those reported in [5][6]. However, these methods often require the use of special equipment, such as a microwave radiometer as seen in [5], or rely on external meteorological datasets and numerical weather prediction products to estimate clear-sky attenuation as seen in [6]. While effective, these methods introduce additional costs and logistical complexity, and they are prone to outages or calibration issues.

To overcome these dependencies, we propose an event detection algorithm that relies solely on beacon power measurements. The method is based on the comparison between a short-term running average, which follows rapid fluctuations of the received signal, and a long-term running average, which captures the slower baseline variations. When the deviation between the two averages exceeds a predefined threshold ($\boldsymbol{\sigma_{th}}$), the algorithm declares the onset of an attenuation event. Conversely, when the deviation falls below the threshold, the event is considered finished, and the link is assumed to have returned to clear sky conditions. This dual moving-average approach exploits the fact that, at Ka- and Q-band frequencies, rapid drops in received power are strongly associated with cloud and rain attenuation along the link.

The contributions of this paper are threefold. First, we present the dual moving-average event detection algorithm and describe its implementation. Second, we validate the algorithm using one year (2015) of Alphasat Aldo Paraboni beacon data collected at the Italian ground stations Tito Scalo and Spino d'Adda [7], with radiometer-based detections serving as the reference. Third, we evaluate performance in terms of relative error in event duration, overlap with reference events, and first order statistics of excess attenuation. Results show that the proposed method achieves reasonable accuracy without requiring ancillary instrumentation, though calibration of parameters is necessary on a per-link basis.

2. Theory

The principle of the Rain Event Detector (RED) is to exploit the fast deviations of the received signal relative to its slower trend to identify the onset and termination of rainfall events, i.e., moments in which the received power dips due to tropospheric impairments. At each time step, two exponentially weighted running-window averages of the received beacon power are computed; a short-term mean $\overline{\boldsymbol{P_s}}(\boldsymbol{t})$ over a short window of length $\boldsymbol{W_s}$, capturing rapid fluctuation, a long-term mean $\overline{\boldsymbol{P_l}}(\boldsymbol{t})$ over a longer window of length $\boldsymbol{W_l}$, capturing the slowly varying baseline. In general, an exponentially weighted running-window mean over window length $\boldsymbol{W}$ is given by.

$$\overline{\boldsymbol{P}}(\boldsymbol{t}) = \frac{\sum_{i=0}^{W-1} \boldsymbol{\lambda_i} \boldsymbol{P}(\boldsymbol{t}-\boldsymbol{i})}{\sum_{i=0}^{W-1} \boldsymbol{\lambda_i}} \tag{1}$$

where $\boldsymbol{W} \in \{\boldsymbol{W_s}, \boldsymbol{W_l}\}$, $\overline{\boldsymbol{P}}(\boldsymbol{t}) \in \{\overline{\boldsymbol{P_s}}(\boldsymbol{t}), \overline{\boldsymbol{P_l}}(\boldsymbol{t})\}$ and $\boldsymbol{\lambda_i} \in (\boldsymbol{0}, \boldsymbol{1})$ are the weights. In this work the weights are organized in descending order, giving more importance to the most recent time instant so that $\overline{\boldsymbol{P_s}}(\boldsymbol{t})$ is more reactive to the state of the channel. The deviation between the two averages is then defined as:

$$\Delta\boldsymbol{P}(\boldsymbol{t}) = \overline{\boldsymbol{P_s}}(\boldsymbol{t}) - \overline{\boldsymbol{P_l}}(\boldsymbol{t}) \tag{2}$$

An attenuation event is triggered when $\Delta\boldsymbol{P}(\boldsymbol{t}) > \boldsymbol{\sigma_{th}}$, where $\boldsymbol{\sigma_{th}}$ is a predefined deviation threshold. Once an event is triggered, the long-window average acts as a persistence function, holding its last clear-sky value to serve as a stable reference throughout the duration of the event. This prevents the baseline from drifting with the short-term fluctuations acting as a fictitious clear sky reference, which is utilized for the calibration procedure. The event remains active until $\Delta\boldsymbol{P}(\boldsymbol{t})$ drops back below $\boldsymbol{\sigma_{th}}$, indicating that the short- and long-term averages have reconverged, and the signal has returned to near clear-sky conditions. When the event ends the long-window average is reset to resume computation over all subsequent non-event samples, re-establishing the clear-sky baseline. By tuning the parameters ($\boldsymbol{W_s}, \boldsymbol{W_l}, \boldsymbol{\sigma_{th}},$), the algorithm can balance sensitivity and robustness, with detected deviations corresponding to cloud and rain induced attenuation on the SatCom link.

The proposed algorithm is inspired by the observation that attenuation dynamics at frequencies such as Ka and Q occur at multiple different rates. Under clear-sky conditions, beacon signal variations are dominated by slow drifts due to gaseous absorption, and system effects (EIRP, component aging, temperature effects etc.) [5]. Consequently, during these conditions, the short-term and long-term running averages of the received power remain closely aligned. During attenuation events, however, rainfall and clouds introduce rapid increases in attenuation that affect the received power signal. Provided the averaging windows are defined well enough, where W_L is large enough to smooth out fast dynamics and W_s small enough to capture the dynamics, the presence of rain and clouds translates to a deviation between the two averaged power signals. This behavior can also be observed in terms of the fade slope, i.e., the rate of change of attenuation over time. As shown by recent analyses of multi-year Alphasat beacon measurements, fade slopes are typically small under low attenuation but increase sharply during rainfall, especially at higher frequencies [8]. A larger fade slope implies that the short-term moving attenuation average would change much more quickly than the long-term average, because of the smaller memory associated to a small averaging window, as opposed to the greater influence of past values associated to a long averaging window. Thus, by monitoring the divergence between short- and long-term averages, the method effectively captures the onset and termination of attenuation events that can be characteristic of cloud and rain attenuation in Ka- and Q-band links.

3. Experimental methodology and simulation

Experimental methodology

The experiment consists in testing this algorithm on the received beacon power collected during the Alphasat Aldo Paraboni propagation experiment [7]. The Italian segment of the propagation campaign, which began in 2015, consist of two ASI ground stations in Italy, one at Tito Scalo and the second at Spino d'Adda. The ground stations measure the received power of two continuous wave beacon signals located onboard the Alphasat geosynchronous telecommunication satellite. The beacons transmit at 19.7 GHz (Ka band) and 39.4 GHz (Q band). The two Italian ground stations are composed of a beacon receiver, a 4.2 m parabolic antenna, meteorological sensors, tipping bucket rain gauge and a microwave radiometer (MWR). The data collected at the stations has been and is being (campaign is ongoing) processed using MWR observations. The calibration procedure, detailed in [5][7][8], consists in identifying rain events occurring along the signal trajectory. The detection algorithm, called Sky Status Indicator (SSI), uses a ratio between brightness temperatures observed at 23.8 GHz and 31.4 GHz to indicate the probable presence of rain [9]. The final step of the processing, defined in [5][7][8], is to eliminate any anomalies in the attenuation timeseries that have non-tropospheric origins such as, antenna tracking malfunction, loss of lock with the beacon and spurious spikes in received power. The result is a polished dataset of total tropospheric attenuation, which will be our reference dataset.

For the development of RED, a preliminary processing of the received power signal was necessary to focus on the algorithm's capability of detecting rain events. This includes two steps. The first, days were collapsed into monthly timeseries down sampled from a sampling frequency of 16 Hz (1 sample every 0.0625 seconds) to 1/15 Hz, corresponding to 1 sample every 15 seconds. The reason for the down sampling to 15 seconds was to reduce the computational cost, whilst ensuring fast rain variations were still included, considering the 1-minute upper limit [10]. The second step ensures comparable dataset sizes, by exploiting the flagged anomalies in the calibrated timeseries, to pre-polish the received beacon power timeseries. Fig. 1 shows the calibrated attenuation timeseries for a particular day and the concurrent unpolished received power. The green sections indicate time instants in the received power, that are removed. After the preprocessing the detection algorithm is applied.

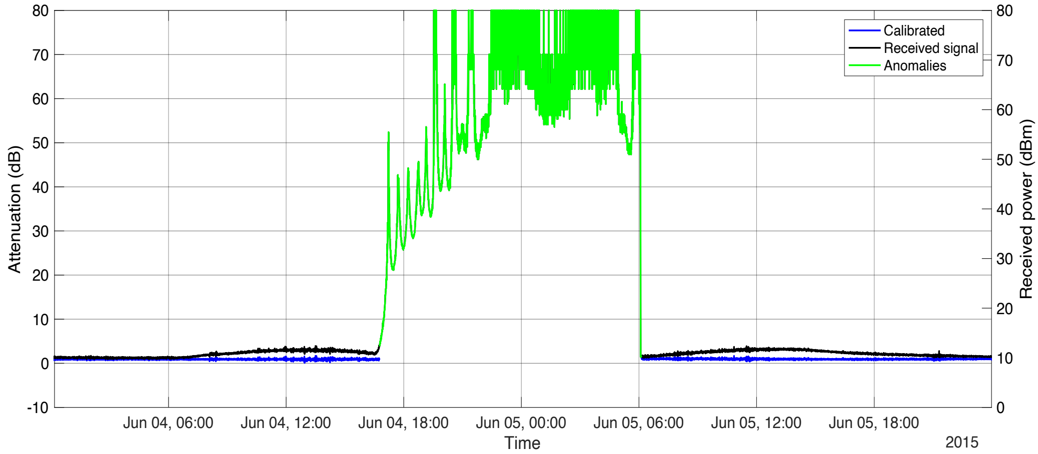

Fig. 1: Sample timeseries of the 'polishing' of the received beacon power (black) using the previously calibrated beacon signal (blue). The green indicates the system outage that is removed.

Simulation

The algorithm is applied to each month in sequence. The moving average windows start at time $t = 0$ of the month and progress in time creating the two signals: the reference signal, $\overline{\boldsymbol{P}_l}(t)$, and the detection signal, $\overline{\boldsymbol{P}_s}(t)$. An example of the moving windows is depicted in the top right corner of Fig. 2 where the blue box indicates all the observation points in $\boldsymbol{W}_s$ and the red one indicates all the observation points in $\boldsymbol{W}_l$. For this article, windows of 1800 seconds and 60 seconds were used respectively for $\boldsymbol{W}_l$ and $\boldsymbol{W}_s$. Thirty minutes were chosen to ensure that only slow varying effects were considered in the creation of the reference signal. Whereas one minute was chosen for $\boldsymbol{W}_s$ as it is small enough to retain the dynamic characteristics of rain [10], but long enough to filter out noise. Fig. 2 shows an example of how the algorithm operates, where the black line is the received power (after pre-processing), the red line is the general trend obtained from the large running window and the blue line is the small running moving average, which closely follows the black line. The light blue dotted line indicates the detection of an event. Note that as the event ends ($\Delta \boldsymbol{P}(\boldsymbol{t}) < \boldsymbol{\sigma_{th}}$), the trend (red) line jumps from the persisted value to the trend of the signal after the event, updating the baseline of attenuation to clear sky conditions after the event.

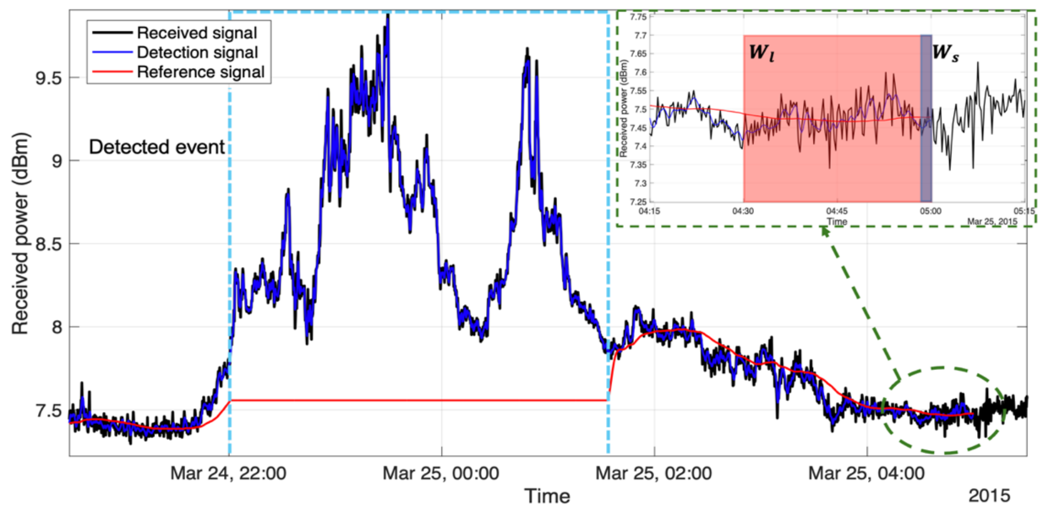

Fig. 2: Diagram of event detection algorithm operation. Black line is the received power signal, blue is the detection signal, red is the reference (or trend) signal. The embedded figure in the top right shows how the moving averages run along the input timeseries signal. Light blue dotted line indicates detected event.

To evaluate the success of the simulation, the events detected by RED defined as D_E are compared against the confirmed events C_E provided by the reference dataset calibrated via SSI and visual inspection. Using these parameters, two KPIs are specified for the evaluation on the effectiveness of RED when compared to our reference dataset. The first one is the percentage overlap (Π), which is the ratio of total seconds of overlap (T_{OP}) between D_E and C_E (refer to patterned boxes in Fig. 3) to the total seconds of confirmed events (T_{CE}) as displayed in (3).

$$\Pi = \frac{T_{OP}}{T_{CE}} \cdot 100\% \tag{3}$$

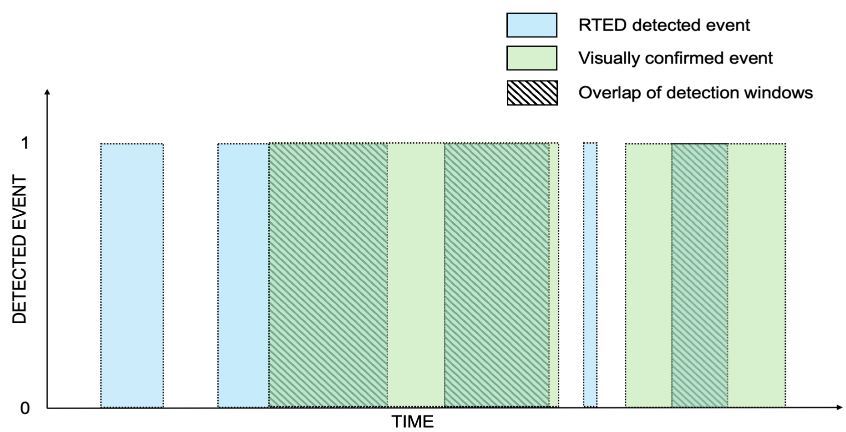

Fig. 3: Schematic showing the definition of T_{DE}, T_{CE} and T_{OP}.

The second, shown in (4), is the ratio ρ of relative difference between total seconds of D_E (T_{DE}) and T_{CE} to T_{CE}.

$$\rho = \frac{T_{CE} - T_{DE}}{T_{CE}} \cdot 100\% \quad (4)$$

Referring to Fig. 3, the sum of the turquoise box areas and the sum of the green box areas represent T_{DE} and T_{CE} , respectively. The patterned boxes are equal to the overlap between turquoise and green area, which is the time where D_E are concurrent with C_E (defined as T_{OP}).

The KPIs together give an indication of the performance of the detection algorithm. Π is a measure of how concurrent D_E are with respect to C_E; the higher the value the better RED is at finding the same events detected in the reference dataset. The second parameter, ρ, measures the number of seconds identified as an event by the algorithm compared to C_E. This gives an indication of the algorithm's sensitivity to detecting events, a negative value corresponds to over detection, i.e. many more events are identified, and a positive value indicates under detection. Values close to zero indicate that the algorithm identifies a similar quantity of events. The ideal outcome is a high Π and a ρ close to zero, indicating that a similar number of events has been identified and most of these are concurrent with the confirmed events.

5. Results and discussion

The threshold $\boldsymbol{\sigma_{th}}$ was selected through trial and error. The parameters $\mathbf{\Pi}$ and $\boldsymbol{\rho}$ were used to identify the most suitable value for the threshold at each frequency. The RED was applied to the 2015 data collected at Spino d'Adda and Tito Scalo. During the calibration of this year 152 attenuation events, for a total of 603.8 hours of events were identified at Spino d'Adda. After multiple tests, excluded here for brevity, the optimal values of $\boldsymbol{\sigma_{th}}$ at Spino d'Adda are presented in Table 1. During the testing it was observed that the lower the threshold, the greater the $\mathbf{\Pi}$, but at the cost of an over estimation of events (very negative $\boldsymbol{\rho}$). Conversely, a high threshold only detects the intense events, also missing the milder instants of the same event, hence providing a low $\mathbf{\Pi}$. Therefore, it was necessary to find a good compromise between the two parameters.

Table 1: Best performing RED thresholds at Spino d'Adda and Tito Scalo for 2015. At Tito Scalo only months from March to December were considered.

	Ka band				Q band			
	σ_{th} (dBm)	No. D_E events	Π (%)	ρ (%)	σ_{th} (dBm)	No. D_E events	Π (%)	ρ (%)
Spino d'Adda	0.25	388	58.97	0.084	0.6	336	64.34	-9.33
Tito Scalo	0.225	318	61.28	3	0.5	278	65.35	5.48

To further evaluate the algorithm's operability, the excess attenuation, calculated as the difference between the reference signal $\overline{\boldsymbol{P_l}}(\boldsymbol{t})$ and the detection signal $\overline{\boldsymbol{P_s}}(\boldsymbol{t})$, according to (5), was compared to the excess attenuation obtained from the reference dataset $\boldsymbol{A_{exc}^{cal}(t)}$. In (5) the received power was initially inverted to create a positive received power from, which the attenuation was calculated.

$$\boldsymbol{A_{exc}(t) = -\left(\overline{P_s}(t) - \overline{P_l}(t)\right)} \quad (5)$$

The comparison of the Complementary Cumulative Distribution Functions (CCDFs) between $\boldsymbol{A_{exc}(t)}$ and $\boldsymbol{A_{exc}^{cal}(t)}$ is presented in Fig. 4 for both frequencies. Only the attenuation within the identified events was considered, while the attenuation outside of the events was set to 0 dB. The CCDFs, given by $\boldsymbol{P(A > A_{th})}$, were developed using the attenuation thresholds specified in the ITU-R DBSG3 tables where $\{\mathbf{0.001\ dB} \le \boldsymbol{A_{th}} \le \mathbf{100}\ \boldsymbol{dB}\}$. Overall, by directly applying the RED and calculating the excess attenuation it is possible to closely reproduce the excess attenuation that was observed for Spino d'Adda during 2015. The zoomed section in the figure highlights the percentage probability of rain. It shows that with the selected thresholds the percentage probability of rain is slightly underestimated from 6% at both frequencies for $\boldsymbol{A_{exc}^{cal}}$ to 4.5% at Ka and 5% at Q bands for $\boldsymbol{A_{exc}}$.

Ideally there should be a perfect match, however because of some imprecisions in the detection of events and in the creation of the reference signal, $\boldsymbol{A_{exc}(t)}$ can either be underestimated or overestimated with respect to $A_{exc}^{cal}(t)$, thus producing some differences between the curves. These imprecisions are exposed in Fig. 5 and Fig. 6. In the first example (Fig. 5) the RED event windows (green boxes) are limited in extent causing the $\overline{P_l}(t)$ to follow $\overline{P_s}(t)$ more closely such that when (5) is applied, the excess attenuation is lower than it should be. Furthermore, since the RED windows are smaller than the confirmed windows (magenta boxes), in the derivation of the CCDFs fewer sample points are available, affecting the statistic.

Alternatively, Fig. 6 displays the case where the attenuation can be overestimated. Purely based on the received signal, any increments in power can be considered as an event if the threshold condition is satisfied. This is the case for the 25th of July 2015 between 00:00 and 1:00, the peak is included in the event window, which during the calibration with the radiometer and rain gauge was confirmed to not belong to the event. As a result, this overestimation, if of frequent occurrence, influences the CCDF. However, Fig. 6 is also an example of the true potential of RED, that is, while it detects the presence of the event it can simultaneously provide an estimate of the excess attenuation (black line) which in this case follows well the one obtained from the reference dataset (cyan line).

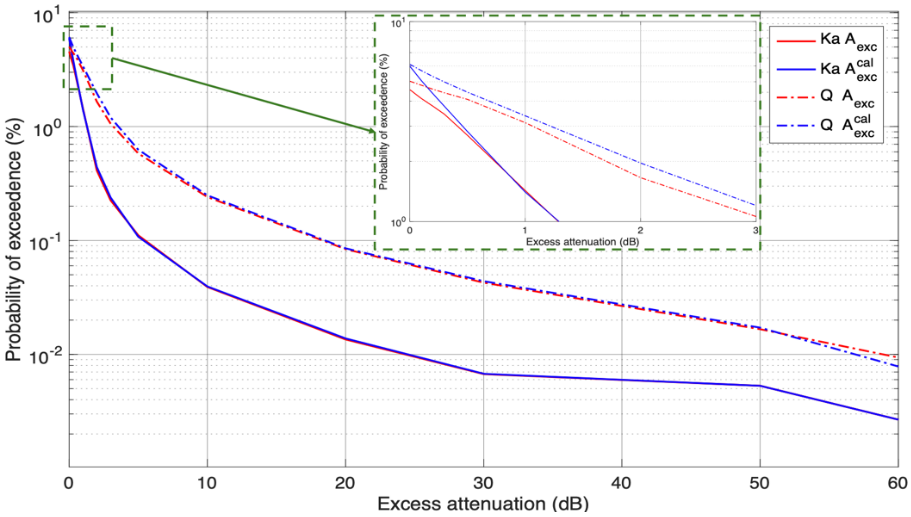

Fig. 4: CCDF of excess attenuation, at Spino d'Adda, calculated from (5) (red lines) and compared to the excess attenuation derived from signal calibration (blue lines). Full lines refer to 19.7 GHz and dash-dotted to 39.4 GHz beacons.

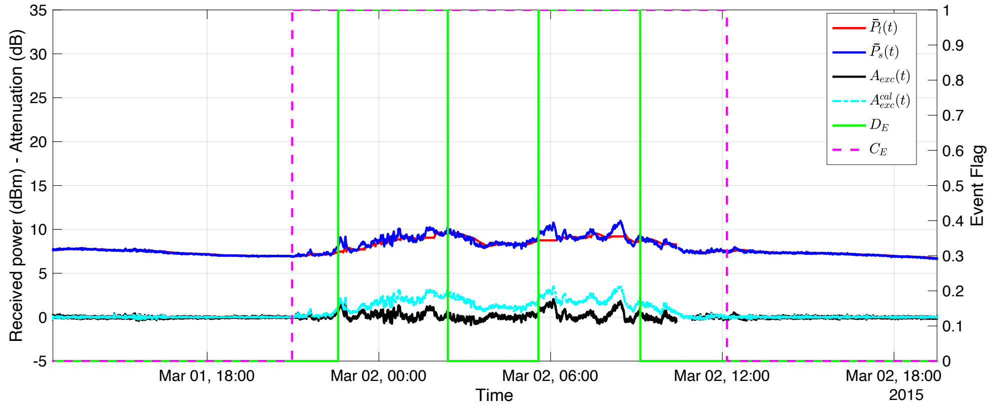

Fig. 5: Example of imprecise event selection for Q band beacon. Green boxes are RED windows, and magenta dashed boxes are visually confirmed event windows.

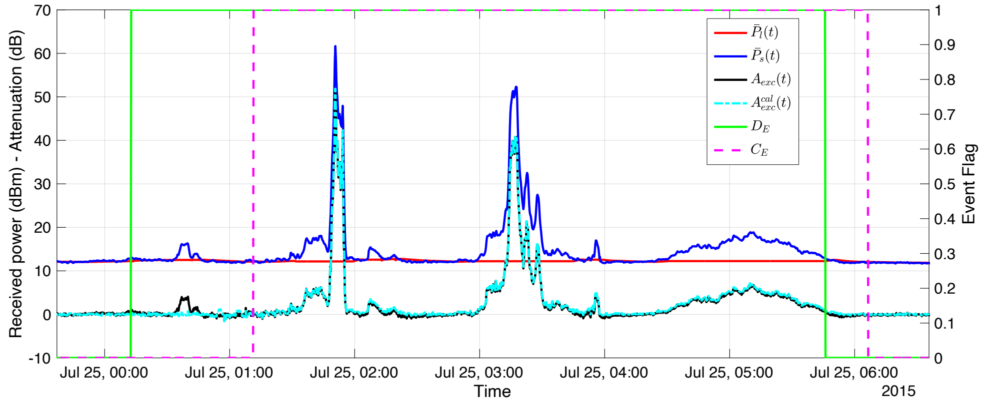

Fig. 6: Example of window selection by RED with an over estimation of excess attenuation at the beginning of event.

The same approach was applied to the station of Tito Scalo. However, because of frequent and strong instabilities in the received signal, for 2015 only the months from March to December were considered. The reduced dataset is composed of 121 rain events for a total of 463.95 hours of rain. Table 1 reports the best deviation thresholds (σ_{th}) and the KPI's used to assess the overall performance with respect to the refence dataset. The most obvious difference is the threshold level, which is lower compared to the station at Spino d'Adda. This difference could originate in the higher elevation angle of 42.1° observed at Tito Scalo with respect to the 35.5° seen at Spino d'Adda. The higher elevation angle implies a shorter path through the troposphere hence the signal accumulates less attenuation. Therefore, a lower threshold is needed to identify the events. The comparison of the excess attenuation CCDFs for Tito Scalo are presented in Fig. 7. Differently from Fig. 4, there is a higher degree of underestimation of the attenuation, particularly for attenuations below 10 dB. The reason is the same as above, $\overline{P_l}(t)$ maintains a larger value, so that when (5) is applied it causes $A_{exc}(t)$ to be underestimated. Despite these criticalities, once the correct thresholds have been identified, RED can detect rain events along the signal trajectory and reproduce the excess attenuation to an acceptable degree.

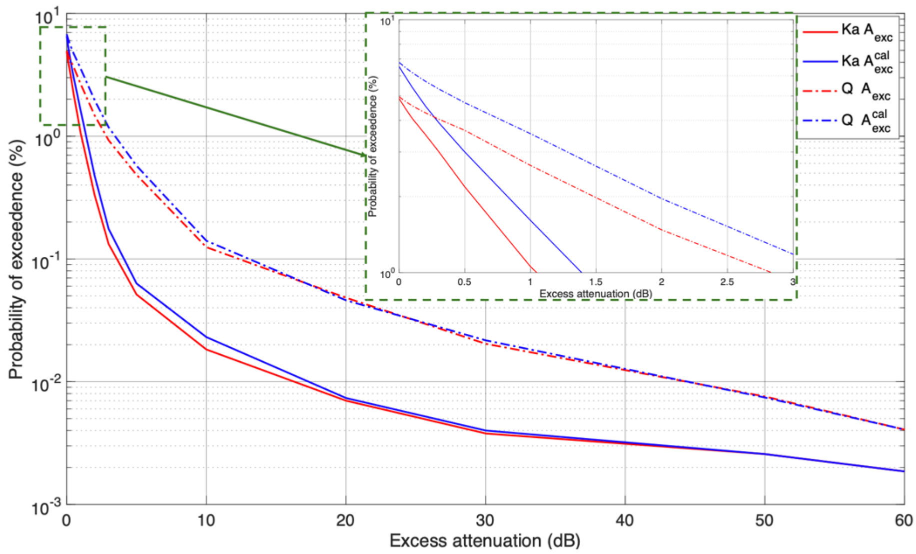

Fig. 7: CCDF of excess attenuation, at Tito Scalo, calculated from (5) (red lines) and compared to the excess attenuation derived from signal calibration (blue lines). Full lines refer to 19.7 GHz and dash-dotted to 39.4 GHz beacons.

5. Conclusion

This work introduced the RED algorithm for event detection and calibration of beacon signals in propagation campaigns. Using only two exponentially weighted moving averages ($\boldsymbol{W_s}$ and $\boldsymbol{W_l}$) and a deviation threshold ($\boldsymbol{\sigma_{th}}$), RED can identify attenuation events due to clouds and rain along the link trajectory without the use of ancillary equipment.

Performance was evaluated against a year of radiometer-calibrated data from Tito Scalo and Spino d'Adda (2015). At Tito Scalo, optimal thresholds ($\boldsymbol{\sigma_{th}}$ equal to 0.225 for Ka, 0.5 for Q) yielded overlaps of 61.3% and 65.4% with confirmed events, with relative differences of 3% and 5.5%, respectively, indicating only slight underestimation. At Spino d'Adda, $\boldsymbol{\sigma_{th}}$= 0.25 (Ka) produced 59% overlap and 0.08% relative difference, while $\boldsymbol{\sigma_{th}}$= 0.6 (Q) achieved 64.3% overlap with a −9.3% difference. In both sites, the CCDF of excess attenuation derived from RED closely matched that of the calibrated reference dataset.

These results demonstrate RED's potential as a robust, low-complexity event detection tool. Future work will address the algorithm's capability to handle anomalies and refine threshold selection through more empirical methods. Furthermore, it will explore the uses on other satellite links at lower elevation angles and higher frequencies and investigate the relationship between the threshold and frequency, elevation and site location.

References

[1] O. Kodheli *et al.*, "Satellite Communications in the New Space Era: A survey and Future Challenges," in *IEEE Communications Surveys & Tutorials,* Vol. 23, No. 1, 2021, pp. 70-109

[2] C. Sacchi *et al.*, "Extremely High Frequency (EHF) Bands for Future Broadcast Satellite Services: Opportunities and Challenges," in *IEEE Transactions on Broadcasting,* Vol. 65, No. 3, 2019, pp. 609-626

[3] Arbesser-Rastburg *et al.,* "COST Action 255 Action 255 Final Report: Radiowave Propagation for SatCom Services at Ku-Band and Above," 2002

[4] "Propagation data and prediction and Prediction methods required for the design of Earth-space telecommunication systems", in *ITU-R P.618-14, P Ser. Recommend. Radiowave Propagation*, 2023, pp. 1-30

[5] L. Luini *et al.*, "Calibration and use of microwave radiometers in multiple-site EM wave propagation experiments," *12th European Conference on Antennas and Propagation (EuCAP 2018)*, London, UK, 2018, pp. 1-5

[6] L. Luini *et al.*, "Methods to Estimate Gas Attenuation in Absence of a Radiometer to Support Satellite Propagation Experiments," in *IEEE Transactions on Instrumentation and Measurement*, vol. 69, no. 7, 2020, pp. 5116-5127

[7] C. Riva *et al.,* "The Alphasat Aldo Paraboni propagation experiment: Measurement campaign at the Italian ground stations," in *Int. J. Satell. Commun. Network* Vol. 37, No. 5, 2019, pp. 423-436

[8] M. Turner *et al.*, "Multiyear Second Order Statistics of ALPHASAT Beacon Measurements at ASI Ground Stations," *2025 19th European Conference on Antennas and Propagation (EuCAP)*, Stockholm, Sweden, 2025, pp. 1-5

[9] A. V. Bosisio et al., "A Sky Status Indicator to Detect Rain-Affected Atmospheric Thermal Emission Observed at Ground", *IEEE Transaction on Geoscience and Remote Sensing*, vol. 51, no. 9, September 2013, page 4643-4649.

[10] L. Luini, "Modeling the Space–Time Evolution of Rain Fields: Electromagnetic wave propagation applications," in *IEEE Antennas and Propagation Magazine*, vol. 63, no. 4, 2021, pp. 12-20